Monthly Notices
of the
ROYAL ASTRONOMICAL SOCIETY

MNRAS **430,** 2932–2942 (2013) doi:10.1093/mnras/stt095

Physical properties of the WASP-44 planetary system from simultaneous multi-colour photometry

L. Mancini,[1]⋆ N. Nikolov,[1] J. Southworth,[2] G. Chen,[1,3] J. J. Fortney,[4] J. Tregloan-Reed,[2] S. Ciceri,[1] R. van Boekel[1] and Th. Henning[1]

[1]*Max Planck Institute for Astronomy, Königstuhl 17, D-69117 Heidelberg, Germany*
[2]*Astrophysics Group, Keele University, Newcastle-under-Lyme, ST5 5BG, UK*
[3]*Purple Mountain Observatory & Key Laboratory for Radio Astronomy, 2 West Beijing Road, Nanjing 210008, China*
[4]*Department of Astronomy & Astrophysics, University of California, Santa Cruz, CA 95064, USA*

Accepted 2013 January 14. Received 2013 January 8; in original form 2012 November 9

ABSTRACT

We present ground-based broad-band photometry of two transits in the WASP-44 planetary system obtained simultaneously through four optical (Sloan g', r', i', z') and three near-infrared (NIR; J, H, K) filters. We achieved low scatters of 1–2 mmag per observation in the optical bands with a cadence of ≈48 s, but the NIR-band light curves present much greater scatter. We also observed another transit of WASP-44 b by using a Gunn r filter and telescope defocussing, with a scatter of 0.37 mmag per point and an observing cadence around 135 s. We used these data to improve measurements of the time of mid-transit and the physical properties of the system. In particular, we improved the radius measurements of the star and planet by factors of 3 and 4, respectively. We find that the radius of WASP-44 b is $1.002 \pm 0.033 \pm 0.018\,R_{\rm Jup}$ (statistical and systematic errors, respectively), which is slightly smaller than previously thought and differs from that expected for a core-free planet. In addition, with the help of a synthetic spectrum, we investigated the theoretically predicted variation of the planetary radius as a function of wavelength, covering the range 370–2440 nm. We can rule out extreme variations at optical wavelengths, but unfortunately our data are not precise enough (especially in the NIR bands) to differentiate between the theoretical spectrum and a radius which does not change with wavelength.

Key words: stars: fundamental parameters – stars: individual: WASP-44 – planetary systems.

1 INTRODUCTION

The *transit method* is not only an excellent technique to detect extrasolar planets, but also provides unrivalled access to their physical parameters. The geometry of a transiting extrasolar planet (TEP) system permits measurement of the mass, radius and density of a planet. These quantities require some input from stellar evolutionary theory, but the planetary surface gravity can be measured directly. A TEP system is therefore a potential *horn of plenty* of physical information on planetary systems (Seager & Sasselov 2000; Sudarsky, Burrows & Pinto 2000; Brown 2001; Hubbard et al. 2001; Seager & Mallén-Ornelas 2003; Sudarsky, Burrows & Hubeny 2003; Charbonneau et al. 2005; Holman & Murray 2005; Winn et al. 2005; Southworth, Wheatley & Sams 2007).

Currently, most of the TEPs discovered by ground-based transit surveys (e.g. Bakos et al. 2012; Beatty et al. 2012; Bryan et al. 2012; Hartman et al. 2012; Hellier et al. 2012; Siverd et al. 2012; Smalley et al. 2012; Penev et al. 2013) are close-in hot Jupiters, because the detection probability for such planets is much greater than for those which are smaller or on wider orbits. Hot Jupiters are also relatively straightforward to detect via the *radial velocity method*, as they induce comparatively large velocity variations in their host stars. The existence of hot Jupiters was unexpected (Mayor & Queloz 1995), and led to the birth of new formation and migration theories (see the reviews of D'Angelo, Durisen & Lissauer 2010; Lubow & Ida 2010). The bias of the ground-based surveys in favour of this class of planets is clear, whereas the *Kepler* satellite has already found hundreds of smaller and longer period planet candidates from only 16 months of data (Borucki et al. 2011a,b; Batalha et al. 2013).

Another fascinating opportunity offered by TEPs is the possibility to probe their atmospheres. Due to atomic and molecular absorption, the analysis of the spectrum of the parent stars during transit (primary eclipse) is an excellent way to probe their atmospheric composition. The existence of two different classes of hot Jupiters (pM and pL) has been suggested according to the incident stellar flux received from the parent star and to the expected amount of absorbing substances, such as gaseous titanium oxide

⋆E-mail: mancini@mpia-hd.mpg.de

(TiO) and vanadium oxide (VO), in their atmospheres (Fortney et al. 2008). According to theoretical models, these two oxidized elements should be extremely strong absorbers for the pM class between 450 and 700 nm, causing such planets to have a hot (∼2000 K) stratosphere. An observable variation of radius with wavelength, due to the opacities of these elements, is consequently expected in the optical bands (Burrows et al. 2007). The radius of a pM planet should be 3 per cent lower at 350–400 versus 500–700 nm. The radius variations for the colder pL-class planets (incident flux $<10^9$ erg s^{-1} cm^{-2}) are smaller, but a significant contribution to the opacity in the optical band is expected from Na I at ∼590 nm, and K I at ∼770 nm (Fortney et al. 2008, 2010; Burrows et al. 2010). Transmission spectroscopy is essential for detecting atmospheric absorbers, and is complementary to observations at secondary eclipse which can help to determine the day-side atmospheric temperature structure.

Accurate measurements of planet radii provide critical constraints for astrophysicists working on planet formation and evolution, because they provide an indication of the planet internal heat, structure and composition, as well as the heating mechanism for those which undergo strong tidal effects and stellar irradiation, allowing the discrimination between competing theories (Pollack et al. 1996; Boss 1997). In particular, the most irradiated hot Jupiters are characterized by anomalously inflated radii for which the explanation remains unclear (Bodenheimer, Laughlin & Lin 2003; Gu, Bodenheimer & Lin 2004; Gaudi 2005; Fortney, Marley & Barneset 2007; Dobbs-Dixon & Lin 2008; Jackson et al. 2008; Batygin, Bodenheimer & Laughlin 2009; Ibgui & Burrows 2009; Miller, Fortney & Jackson 2009; Ibgui, Burrows & Spiegel 2010; Demory & Seager 2011; Laughlin, Crismani & Adams 2011; Miller & Fortney 2011).

Photometric and spectroscopic analyses of planet atmospheres started with the use of optical, near-infrared (NIR) and infrared instruments aboard the *Hubble* and *Spitzer* space telescopes (Charbonneau et al. 2002; Vidal-Madjar et al. 2003, 2004; Richardson et al. 2006, 2007; Knutson et al. 2007a,b; Tinetti et al. 2007; Beaulieu et al. 2008, 2010, 2011; Pont et al. 2008; Swain, Vasisht & Tinetti 2008; Gillon et al. 2012) and led to the detection of Rayleigh scattering in a few hot Jupiter atmospheres, plus absorption lines associated with H_2O, Na, CH_4, TiO and VO (see above references but also Ballester, Sing & Herbert 2007; Barman 2007; Désert et al. 2008, 2011; Lecavelier des Etangs et al. 2008; Sing et al. 2008a,b; Spiegel, Silverio & Burrows 2009; Zahnle et al. 2009; Fossati et al. 2010; Tinetti et al. 2010; Gibson, Pont & Aigrain 2011; Wood et al. 2011; Crossfield et al. 2012; Crouzet et al. 2012).

After a number of pioneering experiments with null results, ground-based spectroscopy also obtained some interesting results. Observations performed at the Hobby–Eberly and Subaru telescopes, in the spectral range 500–900 nm, detected Na absorption in the transmission spectrum of HD 189733 b (Redfield et al. 2008) and HD 209458 b (Snellen et al. 2008). NIR spectroscopy of HD 209458 b at the VLT in the range 2291–2349 nm reported a significant wavelength shift in absorption lines from carbon monoxide in the planet's atmosphere (Snellen et al. 2010).

High-resolution NIR spectroscopic measurements at the Keck telescopes over the wavelength range 2100–2400 nm revealed an upper limit for CO absorption in the atmosphere of HD 209458 b (Deming et al. 2005), and that the super-Earth GJ 1214 b is an H-dominated planet (Crossfield, Barman & Hansen 2011). GJ 1214 b was also studied through multi-object spectroscopy from 0.61 to 0.85 μm, and in the *J*, *H* and *K* atmospheric windows by using VLT/FORS and Magellan/MMIRS, the data being consistent with a featureless transmission spectrum for the planet (Bean et al. 2011).

A radius variation with wavelength was investigated for HD 209458 b by Knutson et al. (2007a) using 10 colour *HST* photometry. Different analyses of these data have given conflicting results (Barman 2007; Knutson et al. 2007a; Sing et al. 2008a; Southworth 2008). An *HST* transmission spectrum of HD 189733 b covering 270–570 nm showed a gradual increase of radius towards shorter wavelengths which was interpreted as a result of Rayleigh scattering from a high-altitude atmospheric haze (Sing et al. 2011a). But observations covering 550–1050 nm did not provide any indication of the expected Na I or K I features (Pont et al. 2008), and those in the ranges 1082–1168 and 1514–1693 nm did not detect any variation in planetary radius (Gibson et al. 2012).

Using the Gran Telescopio Canarias (GTC), Sing et al. (2011b) claimed the first evidence for potassium in an extrasolar planet, from photometry of the XO-2 system in four narrow red optical passbands, by detecting K I absorption at 766.5 nm. This technique was also used by Colón et al. (2012) to study HD 80606 b, who found an unexplained large (≈4.2 per cent) change in the apparent planetary radius between the wavelengths 769.9 and 777.4 nm. The differential spectrophotometry technique was used to obtain two transit light curves of XO-2 b with GTC by Sing et al. (2012), who detected significant absorption in the planetary atmosphere in a 50 Å bandpass centred on the Na I doublet. Instead, the presence of an Na-rich atmosphere in WASP-29 b was recently ruled out by Gibson et al. (2013), using Gemini-South GMOS transit spectrophotometry.

Southworth et al. (2012b) recently presented a study of possible radius variations of the hot Jupiter HAT-P-5 b, based on photometry obtained simultaneously in the *u*, *g*, *r* and *I* passbands. The authors detected a gradual increase of the radius between 450 and 850 nm, plus a substantially larger planetary radius at 350 nm. The latter phenomenon can be explained by systematic errors in the *u*-band photometry, but is also consistent with Rayleigh scattering as in the case of HD 189733 b. A similar multi-band investigation of HAT-P-8 (Mancini et al. 2013) suggests the presence of strong optical absorbers near the terminator of this TEP.

Here we focus our attention on the planetary system WASP-44, discovered by Anderson et al. (2012). The system consists of a 0.89 $M_{\rm Jup}$ planet on a 2.42 d orbit around an inactive G8 V star ($V = 12.9$, [Fe/H] $= +0.06$). In this work we present the first photometric follow-up since its discovery was announced, covering seven optical/NIR passbands. We refine the physical properties of the system and attempt to probe for radius variations in these passbands.

Our paper is structured as follows. In Section 2, we describe the instruments used for the observations and give some details concerning the data reduction. In Section 3, we illustrate the analysis of the data which led to the refinement of the orbital period and the physical properties of the WASP-44 system. Then, we examine the variation of the planetary radius with wavelength. Finally, in Section 4 we summarize our results.

2 OBSERVATIONS AND DATA REDUCTION

Two transits of WASP-44 b were recorded on 2011 October 2 and 6, using the Gamma-Ray Burst Optical and Near-Infrared Detector (GROND) instrument mounted on the MPG[1]/European Southern Observatory (ESO) 2.2 m telescope at ESO La Silla, Chile. GROND is an imaging system capable of simultaneous photometric observations in four optical (identical to Sloan g', r', i', z') and three

[1] Max Planck Gesellschaft.

Table 1. Log of the observations presented in this work. N_{obs} is the number of observations and 'Moon illum.' is the fractional illumination of the Moon at the mid-point of the transit. The aperture sizes are the radii of the software apertures for the star, inner sky and outer sky, respectively. β is the factor used to inflate the error bars (see Section 3). Transit #1 was observed using the 2.5 m INT in La Palma, whereas transits #2 and #3 using the MPG/ESO 2.2 m telescope in La Silla.

Transit	Date	Start/end time (UT)	N_{obs}	Exposure time (s)	Filter	Airmass	Moon illum.	Aperture sizes (pixel)	Scatter (mmag)	β
1	2011-09-03	00:28–00:57	156	120	Gunn r	1.60 → 1.32 → 2.18	31 per cent	25, 35, 50	0.37	1.15
2	2011-10-02	03:21–07:35	317	20	Sloan g'	1.08 → 1.05 → 1.54	40 per cent	16, 35, 55	1.23	1.07
2	2011-10-02	03:21– 07:35	317	20	Sloan r'	1.08 → 1.05 → 1.54	40 per cent	17, 40, 60	1.08	1.00
2	2011-10-02	03:21–07:35	317	20	Sloan i'	1.08 → 1.05 → 1.54	40 per cent	20, 30, 45	1.34	1.00
2	2011-10-02	03:21–07:35	317	20	Sloan z'	1.08 → 1.05 → 1.54	40 per cent	12, 25, 40	1.79	1.10
2	2011-10-02	03:21–07:35	631	3	J	1.08 → 1.05 → 1.54	40 per cent	6.0, 15.0, 23.0	7.66	1.09
2	2011-10-02	03:21–07:35	631	3	H	1.08 → 1.05 → 1.54	40 per cent	2.5, 11.5, 21.0	8.11	1.08
2	2011-10-02	03:21–07:35	631	3	K	1.08 → 1.05 → 1.54	40 per cent	3.0, 11.0, 21.0	5.98	1.15
3	2011-10-06	03:21–07:35	317	25	Sloan g'	2.07 → 1.05	80 per cent	19, 30, 50	1.89	1.06
3	2011-10-06	03:21–07:35	313	25	Sloan r'	2.07 → 1.05	80 per cent	22, 40, 60	1.70	1.32
3	2011-10-06	03:21–07:35	313	25	Sloan i'	2.07 → 1.05	80 per cent	20, 40, 60	1.79	1.35
3	2011-10-06	03:21–07:35	313	25	Sloan z'	2.07 → 1.05	80 per cent	16, 40, 60	2.52	1.26
3	2011-10-06	03:21–07:35	623	3	J	2.07 → 1.05	80 per cent	9.0, 17.0, 25.0	5.23	1.38
3	2011-10-06	03:21–07:35	623	3	H	2.07 → 1.05	80 per cent	6.5, 13.5, 22.0	6.96	1.34
3	2011-10-06	03:21–07:35	623	3	K	2.07 → 1.05	80 per cent	3.5, 4.5, 18.0	7.65	1.04

NIR (J, H, K) passbands (Greiner et al. 2008). Each of the four optical channels is equipped with a back-illuminated 2048 × 2048 E2V CCD, with a field of view (FOV) of 5.4 arcsec × 5.4 arcsec at a scale of 0.158 arcsec pixel^{-1}. The three NIR channels use 1024 × 1024 Rockwell HAWAII-1 arrays with an FOV of 10 arcmin × 10 arcmin at 0.6 arcsec pixel^{-1}.

We applied a slight telescope defocus and obtained repeated integrations during both runs. Autoguiding was used to keep the stars on the same pixels. All images were digitized using the fast readout mode (∼10 s) to improve the time sampling. On 2011 October 2 we monitored the flux of WASP-44 in nearly photometric conditions, and observed a monotonic seeing decline from 0.50 to 1.03 arcsec as airmass decreased from 1.08 to 1.05 and then increased to 1.54. Exposures of 20 s were used in the optical channels and stacks of four 4 s images were obtained in the NIR channels. On 2011 October 6 we experienced worse atmospheric conditions, and the airmass changed from 2.07 to 1.05 during our observations. Images with exposure times of 25 s were obtained in the optical channels, and stacks of six 4 s images were obtained in the NIR channels. For the optical frames we selected a fast readout mode, which provided a 15 s readout. Due to the necessary synchronization of the optical and NIR starting times for each exposure, the observing cadence resulted to be of ≈48 and ≈25 s in the optical and NIR bands, respectively.

Another full transit of WASP-44 b was observed through a Gunn r filter on the night of 2011 November 2 using the Wide Field Camera (WFC) on the 2.5 m Isaac Newton Telescope (INT) at La Palma. WFC is an optical mosaic camera consisting of four thinned EEV 2k × 4k CCDs, with a plate scale of 0.33 arcsec pixel^{-1}. The telescope was heavily defocussed so the point spread function of the target and comparison stars had not more than 35 000 counts pixel^{-1}. We used the fast readout mode to reduce the readout time down to about 15 s. An exposure time of 2 min per frame was used, and the resulting observing cadence was roughly 135 s. The night was photometric. We were not able to autoguide the telescope as the autoguider is incorporated into the WFC and so was also defocussed. A summary of the observational data is reported in Table 1.

Reduction of the optical frames was undertaken using standard methods. We created master bias and flat-field images by median-combining sets of bias images and sky flats, and used them to correct the science images. Aperture photometry was performed using the IDL[2]/ASTROLIB[3] implementation of DAOPHOT (Stetson 1987; Southworth et al. 2009). The apertures were placed manually and shifted to account for pointing variations, which were measured by cross-correlating each image against a reference image. We experimented with wide range of aperture sizes and retained those which gave photometry with the lowest scatter compared to a fitted model. The times of observation were converted from UTC to BJD (TDB) using the IDL procedures of Eastman, Silverd & Gaudi (2010).

Differential photometry was obtained in each filter using between two and four comparison stars, two of which were bright enough to produce count rates comparable to those of WASP-44. All good comparison stars were combined into one ensemble by weighted flux summation. Slow variations in the apparent brightness of the reference stars, primarily attributable to atmospheric effects, were treated by fitting a polynomial to regions outside transit, whilst simultaneously optimizing the weights of the comparison stars. Given the limited number of comparison stars in the small FOV of GROND, and the shape of the slow brightness variations, we used a second-order polynomial versus time. Uncertainties introduced by this procedure were considered in the modelling of the light curves, as described in the next section.

The NIR frames were also calibrated in a standard way, including dark subtraction, flat correction and sky subtraction. The master sky images used in sky subtraction were created from two sets of 20-position dithering sky measurements, one before the science observation and one after. We performed aperture photometry on the calibrated NIR images as well. The aperture locations were determined using IDL/FIND. Various combinations of aperture and annulus sizes were checked to find the best photometry. We also carefully made ensembles of comparison stars, and chose the group which showed the least deviation from the target. After normalizing the target light curve with the composite reference light curve, we decorrelated the data with position, seeing and airmass in order to

[2] The acronym IDL stands for Interactive Data Language and is a trademark of ITT Visual Information Solutions. For further details, see http://www.ittvis.com/ProductServices/IDL.aspx.
[3] http://idlastro.gsfc.nasa.gov/

Table 2. Excerpts of the light curves of WASP-44. The full data set will be made available at the CDS.

Telescope	Filter	BJD (TDB)	Diff. mag.	Error
INT	Gunn r	245 5807.576 418	0.000 36	0.000 41
INT	Gunn r	245 5807.579 370	0.000 09	0.000 42
ESO 2.2 m	Sloan g'	245 5836.647 443	0.001 26	0.001 00
ESO 2.2 m	Sloan g'	245 5836.649 992	0.002 10	0.001 23
ESO 2.2 m	Sloan r'	245 5836.647 443	−0.000 97	0.000 88
ESO 2.2 m	Sloan r'	245 5836.649 992	0.000 79	0.001 09
ESO 2.2 m	Sloan i'	245 5836.647 443	0.000 96	0.001 09
ESO 2.2 m	Sloan i'	245 5836.649 992	0.001 38	0.001 34
ESO 2.2 m	Sloan z'	245 5836.647 443	−0.001 43	0.001 42
ESO 2.2 m	Sloan z'	245 5836.649 992	0.001 00	0.001 79

remove the correlated red noise. We extracted the optimal NIR light curves for the two nights according to the rms of O−C residuals and consistency of the transit depth between two nights. Details are given in Appendix A. The resulting photometry is given in Table 2.

Although we have performed all the possible calibrations and corrections, the scatter of the NIR data is much larger than that of the optical data, and the NIR light curves are heavily dominated by red noise. This problem is related to the adopted observing strategy that unfortunately did not allow a good SNR to be obtained.[4]

Our analysis also included the data set presented by Anderson et al. (2012), which was obtained through a Gunn r filter and using EulerCam mounted on the 1.2 m Euler-Swiss telescope at ESO La Silla.

3 ANALYSIS

We have measured the physical properties of the WASP-44 planetary system following the methodology of the *Homogeneous Studies* project (Southworth 2008, 2009, 2010, 2011, 2012). We refer the reader to those works for a detailed description of the approach.

Since the absolute values of the observational errors from our pipeline (which come ultimately from the APER subroutine) were found to be underestimated, we adopt the standard practice of rescaling them for each data set to give a reduced χ^2 of $\chi^2_\nu = 1$. Then, in order to account for time-correlated errors (i.e. red noise, which can significantly affect ground-based data) and derive more realistic uncertainties, we inflated the error bars further by multiplying the data weights by a factor $\beta \geq 1$. The β approach (e.g. Pont, Zucker & Queloz 2006; Winn et al. 2007) is a widely used way to assess red noise (e.g. Gillon et al. 2006; Gibson et al. 2008; Winn et al. 2008, 2009; Nikolov et al. 2012; Southworth et al. 2012a,b). The factor β is a measurement of how close the data noise is to the Poisson approximation, and is found by binning the data and evaluating the ratio between the size of the residuals versus what would be expected if the data followed Poisson statistics. We evaluated the values of the β factor for each individual transit and for groups of 10 data points; they are reported in Table 1. For a more exhaustive discussion about rescaling error bars, see Andrae (2010).

[4] After these first observations, we changed our observing strategy adopting the *defocussing* technique for GROND. Thanks to this approach, we can now obtain a scatter smaller than 2 mmag per observation in the NIR bands and smaller than 1 mmag in the optical ones, without compromising the sampling (Nikolov et al. 2013).

Table 3. Central transit times of WASP-44 and their residuals versus the ephemeris derived in this work. TRESCA refers to the 'TRansiting ExoplanetS and CAndidates' website.

Central transit time BJD (TDB) − 2400000	Cycle no.	Residual (JD)	Reference
55 434.376 37 ± 0.000 40	0	−0.000 05	Anderson et al. (2012)
55 453.766 39 ± 0.000 42	8	−0.000 54	Anderson et al. (2012)
55 807.643 74 ± 0.000 13	154	0.000 07	This work (INT r)
55 814.916 55 ± 0.001 50	157	0.001 44	Evans P. (TRESCA)
55 829.454 89 ± 0.002 45	163	−0.003 10	Lomoz F. (TRESCA)
55 829.461 51 ± 0.001 63	163	0.003 15	Lomoz F. (TRESCA)
55 836.729 05 ± 0.000 20	166	−0.000 38	This work (GROND g')
55 836.729 79 ± 0.000 30	166	0.000 36	This work (GROND r')
55 836.729 00 ± 0.000 20	166	−0.000 43	This work (GROND i')
55 836.729 28 ± 0.000 15	166	−0.000 15	This work (GROND z')
55 841.577 19 ± 0.000 35	168	0.000 14	This work (GROND g')
55 841.577 57 ± 0.000 46	168	0.000 52	This work (GROND r')
55 841.576 84 ± 0.000 28	168	−0.000 21	This work (GROND i')
55 841.577 69 ± 0.000 31	168	0.000 64	This work (GROND z')
56 127.586 24 ± 0.000 48	286	−0.000 78	Sauer T. (TRESCA)

3.1 Period determination

As a first step, we fitted each light curve individually using the JKTEBOP code (see Section 3.2) in order to find the transit times. Their uncertainties were estimated from Monte Carlo simulations. To these we added two timings obtained by Anderson et al. (2012) and four obtained by amateur astronomers, which are available on the TRESCA[5] website (see Table 3). We excluded from this analysis our NIR data since they are much noisier than the optical ones. All timings were placed on BJD (TDB) time system. The resulting measurements of transit mid-points were fitted with a straight line to obtain a new orbital ephemeris:

$$T_0 = \mathrm{BJD(TDB)}245\,5434.376\,42(37) + 2.423\,8133(23) \times E, \quad (1)$$

where E is the number of orbital cycles after the reference epoch [the mid-point of the first transit observed by Anderson et al. (2012)] and quantities in parentheses denote the uncertainty in the final digit of the preceding number. The fit has $\chi^2_\nu = 2.42$, so the uncertainties were increased to account for this. Despite this large χ^2_ν, we do not note any systematic deviation from the predicted transit times. A plot of the residuals around the fit is shown in Fig. 1. Since the number of known observed transits of this planet is still very low, no conclusions can be drawn regarding the existence of any third body in the system.

3.2 Light-curve modelling

The light curves were modelled using the JKTEBOP[6] code. The primary fitted parameters were the sum and ratio of the fractional radii of the star and planet, $r_\mathrm{A} + r_\mathrm{b}$ and $k = r_\mathrm{b}/r_\mathrm{A}$, and the orbital inclination, i. The fractional radii of the components are defined as $r_\mathrm{A} = R_\mathrm{A}/a$ and $r_\mathrm{b} = R_\mathrm{b}/a$, where a is the orbital semimajor axis, and R_A and R_b are the true radii of the two objects. Additional parameters of the fit included the light level outside the transit and the mid-point

[5] The TRansiting ExoplanetS and CAndidates (TRESCA) website can be found at http://var2.astro.cz/EN /tresca/index.php

[6] JKTEBOP is written in FORTRAN77 and the source code is available at http://www.astro.keele.ac.uk/~jkt/

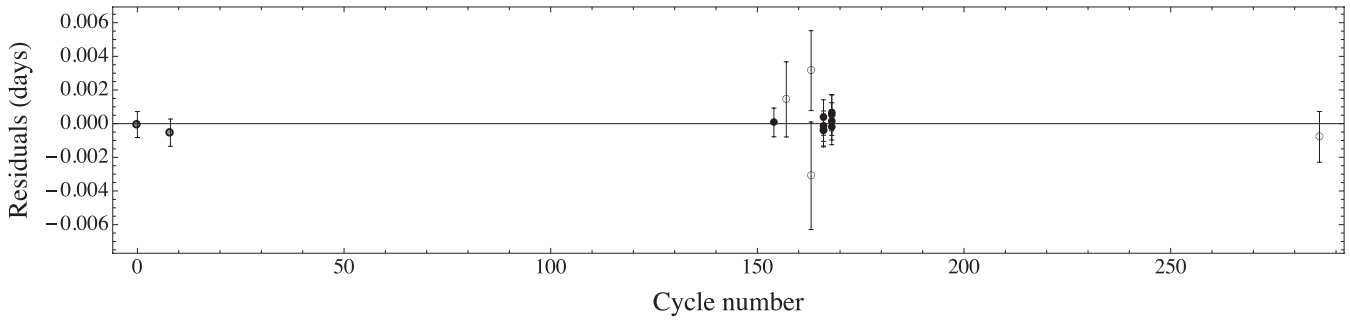

Figure 1. O−C diagram of the mid-transit times of WASP-44 b versus a linear ephemeris. The timings in black are from this work, and in grey are from Anderson et al. (2012). The timings obtained by amateur astronomers are plotted as open circles. The uncertainties of our points have been rescaled (see the text).

Table 4. Parameters of the fits to the 10 light curves of WASP-44. The final parameters are the weighted mean of the result for the GROND, INT and Euler light curves.

Source	$r_A + r_b$	k	$i(^\circ)$	r_A	r_b
GROND g' band #1	0.1368 ± 0.0056	0.1228 ± 0.0023	86.2 ± 0.5	0.1218 ± 0.0020	$0.014\,96 \pm 0.000\,86$
GROND g' band #2	0.139 ± 0.010	0.1188 ± 0.0028	86.2 ± 1.0	0.1240 ± 0.0090	0.0147 ± 0.0014
GROND r' band #1	0.1268 ± 0.0045	0.1175 ± 0.0014	87.3 ± 0.6	0.1135 ± 0.0039	$0.013\,33 \pm 0.000\,60$
GROND r' band #2	0.1284 ± 0.0080	0.1190 ± 0.0029	86.9 ± 0.8	0.1147 ± 0.0068	0.0136 ± 0.0011
GROND i' band #1	0.1363 ± 0.0051	0.1205 ± 0.0016	86.3 ± 0.5	0.1216 ± 0.0044	$0.0147 \pm 0.000\,68$
GROND i' band #2	0.1303 ± 0.0087	0.1204 ± 0.0029	86.7 ± 0.9	0.1163 ± 0.0076	0.0140 ± 0.0011
GROND z' band #1	0.1306 ± 0.0075	0.1153 ± 0.0023	86.8 ± 0.8	0.1171 ± 0.0065	$0.013\,49 \pm 0.000\,95$
GROND z' band #2	0.123 ± 0.010	0.1134 ± 0.0034	87.4 ± 1.5	0.1102 ± 0.0089	0.0125 ± 0.0013
INT r band	0.1285 ± 0.0029	0.1196 ± 0.0013	86.6 ± 0.3	0.1148 ± 0.0026	$0.013\,73 \pm 0.000\,42$
Euler r band	0.141 ± 0.011	0.1197 ± 0.0039	85.9 ± 1.0	0.1261 ± 0.0100	0.0151 ± 0.0016
Final results			$\mathbf{86.59 \pm 0.18}$	$\mathbf{0.1168 \pm 0.0016}$	$\mathbf{0.0139 \pm 0.0002}$
Anderson et al. (2012)	0.1398	0.1260 ± 0.0030	$86.02^{+1.11}_{-0.86}$	0.1242 ± 0.0102	0.0157

of the transit. Limb darkening (LD) was imposed using a quadratic law and the corresponding coefficients were fixed at values theoretically predicted using model atmospheres (Claret 2004). Southworth (2008) performed three different treatments of the LD coefficients: (i) both coefficients fixed to theoretical values, (ii) both coefficients fitted, and (iii) the linear LD coefficient fitted and the non-linear one fixed to its theoretically predicted value. While the second treatment is possible only when the data are of high quality, the use of the third alternative has a negligible impact on the final results. Uncertainties were calculated using both Monte Carlo simulations and a residual-permutation algorithm (Southworth 2008), and the larger of the two values was retained for each output quantity. The orbital eccentricity was fixed to zero (Anderson et al. 2012). All the data sets were solved individually. As in the previous section, due to their large scatter (see Table 1), we did not use the NIR data for estimating the physical properties of the planetary system.

Representative photometric parameters were obtained for each data set and are given in Table 4. The corresponding best fits are shown in Figs 2 and 3 for the GROND data and in Fig. 4 for the INT and Euler data. The final photometric parameters are the weighted mean of the values for each data set. The agreement between light curves is excellent: the χ^2_ν value of the agreement of the individual parameters with respect to the weighted mean is smaller than 0.75 for all except k, where we found a modestly larger χ^2_ν of 1.64. We have found this situation to be common during our work on the *Homogeneous Studies* papers. Table 4 also shows a comparison with the results from Anderson et al. (2012), which are in good agreement with ours but have much larger error bars.

3.3 Physical properties of the WASP-44 system

Following the approach described in Southworth (2009), the estimation of the physical properties of the WASP-44 system was performed making use of a standard formula (e.g. Hilditch 2001). We used the photometric parameters measured in Section 3.2, and the velocity amplitude, effective temperature and metallicity of the star ($K_A = 138.8 \pm 9.0$ km s^{-1}, $T_{\rm eff} = 5410 \pm 150$ K, [Fe/H] $= +0.06 \pm 10$) measured by Anderson et al. (2012). We interpolated within tabulations from theoretical stellar models to find the best agreement between the observed and model-predicted $T_{\rm eff}$, and the measured r_A and calculated R_A/a. This yielded the best-fitting mass, radius, surface gravity and mean density of the star (M_A, R_A, $\log g_A$ and ρ_A) and of the planet (M_b, R_b, g_b and ρ_b). We also calculated the orbital semimajor axis (a), planetary equilibrium temperature ($T_{\rm eq}$), Safranov number (Θ) and the evolutionary age of the star.

The uncertainties in the input parameters were propagated into the output physical properties using a perturbation analysis (Southworth, Maxted & Smalley 2005). Systematic errors were assessed by comparing results from five different sets of theoretical models (see Southworth 2010). The sets of physical properties found using each set of stellar models are shown in Table 5 and the final physical properties of the WASP-44 system are given in Table 6. The results obtained by Anderson et al. (2012) are less precise but are in good agreement with our own. In particular, we improved the measurement precisions of the radii of both the planet and the parent star, by factors of 4 and 3, respectively. The radius of WASP-44 b that we found ($1.002 \pm 0.033 \pm 0.018\,R_{\rm Jup}$) is smaller than that measured

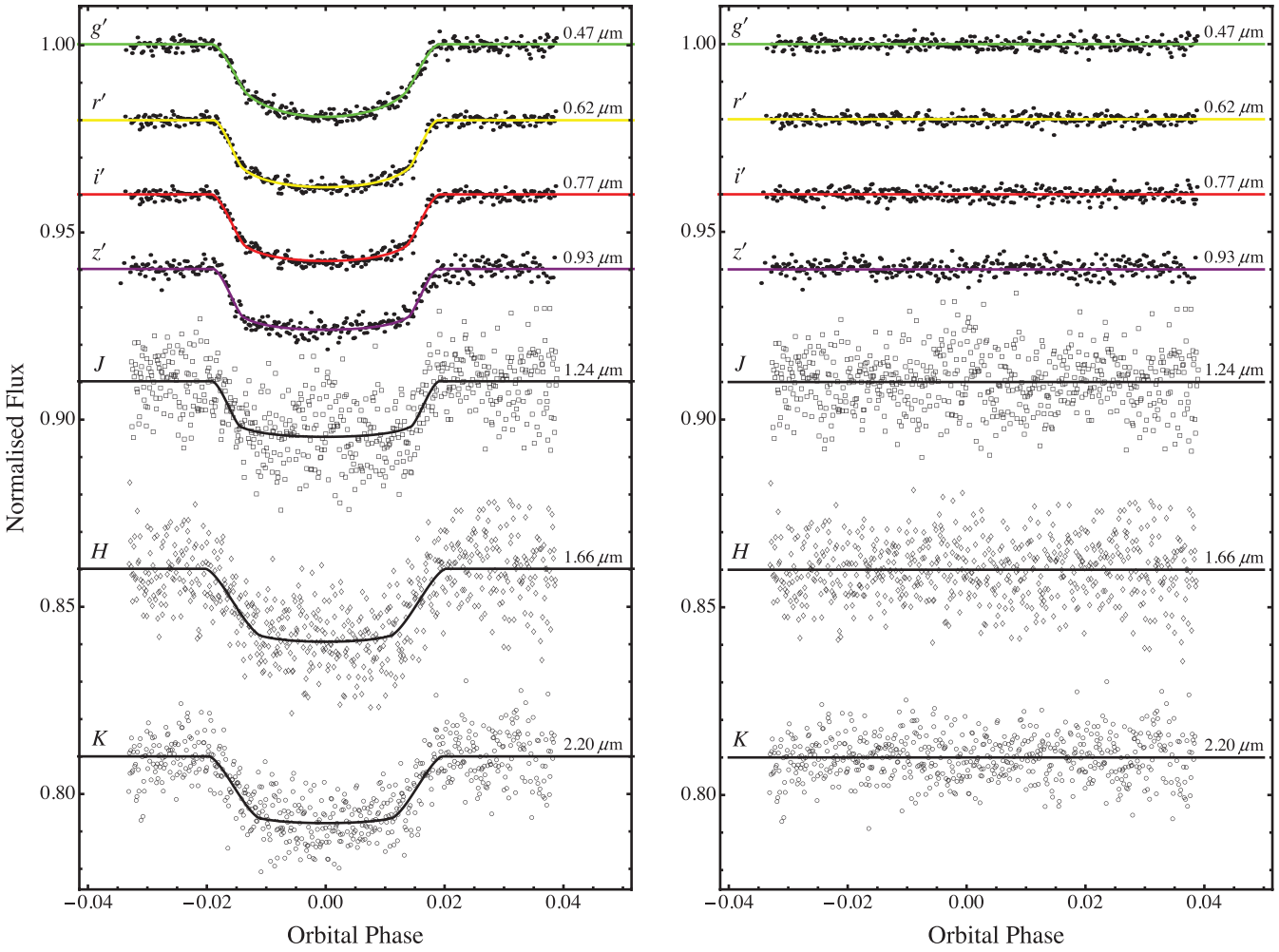

Figure 2. First set (2011 October 2) of GROND light curves of WASP-44 compared to the best JKTEBOP fits using the quadratic LD law. The residuals of the fits are plotted at the base of the figure, offset from zero.

in the discovery paper and does not match the predicted radii of coreless hot Jupiter planets as estimated by Fortney et al. (2007). According to their tables,[7] a 0.875 $M_{\rm J}$ planet with a 50 $M_{\rm Earth}$ core at 0.045 au from the Sun (age 3.16 Gyr) has a radius of 0.991 $R_{\rm Jup}$. On the contrary, the expected radius for a core-free planet with the same properties is 1.119 $R_{\rm Jup}$.

3.4 Variation of planetary radius with wavelength

As an additional possibility for the GROND data, we made an attempt to investigate the possible variation of the radius of WASP-44 b with wavelength. This is quite a difficult task because the relative faintness of the host star ($V \sim 12.9$) makes this system less than ideal for optical photometric studies, especially from the ground. Moreover, as already mentioned, our *in-focus* observing strategy has proved to be ill-suited to obtaining high-precision photometry, particularly in the NIR bands. Finally, by using broad-band filters we are forced to average our measurements of the planet radius in each band over a quite larger range of the wavelength (the best case in the i' filter where its width is 'only' 100 nm). For these reasons, the results of this section should be used with care.

The GROND instrument was conceived only for the follow-up of gamma-ray bursts, and was not designed to allow filter changes for individual observing sequences. We were therefore unable to use filters with narrow passbands covering specific wavelength ranges. We note that the four optical bands of GROND were already used by de Mooij et al. (2012) to investigate the atmosphere of GJ 1214 b, a 6.55 $M_\oplus$ transiting planet. Here we try for the first time to use all the seven bands, exploiting the full potential of GROND.

Following the same strategy used by Southworth et al. (2012b) and Mancini et al. (2013), we proceeded as follows. The two GROND data sets were combined by phase and according to passband, and then fitted with all parameters fixed to the final values given in Table 4, with the exception of k. The LD coefficients were fixed to theoretical values. The errors were estimated by a residual-permutation algorithm (Southworth 2008). This approach removes sources of uncertainty common to all data sets, allowing us to maximize the accuracy of estimations of the fractional planetary radius $r_{\rm b} = R_{\rm b}/a$ as a function of wavelength and with relative error bars only. The results are displayed in Fig. 5, where the points show the data, the vertical bars represent the relative errors in the measurements and the horizontal bars indicate the full width at half-maximum (FWHM) transmission of the passbands

[7] The tables, interpolated from the giant planet thermal evolution models described in Fortney et al. (2007), are available at http://www.ucolick.org/~jfortney/models.htm

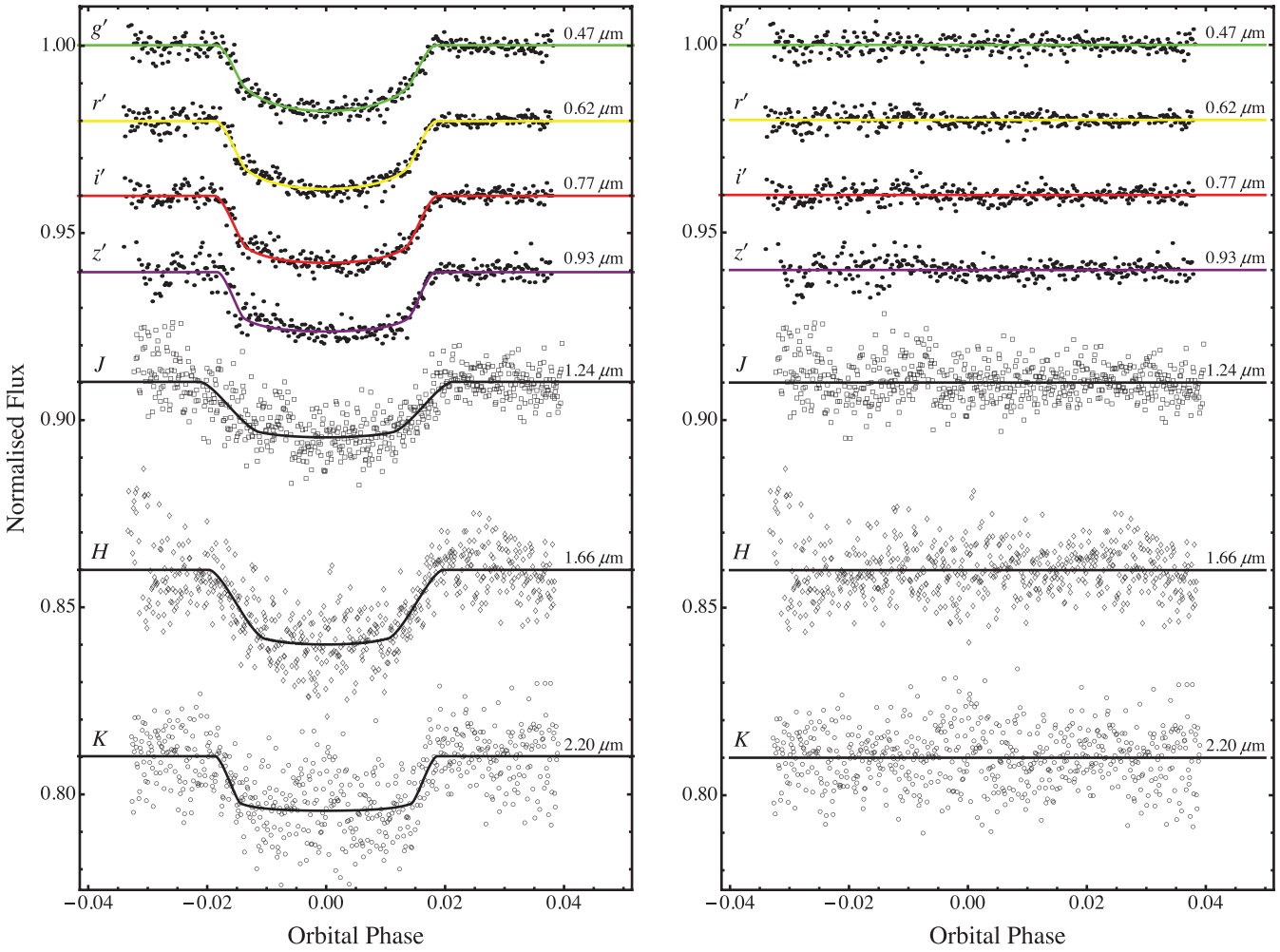

Figure 3. Second set (2011 October 6) of GROND light curves of WASP-44 compared to the best JKTEBOP fits using the quadratic LD law. The residuals of the fits are plotted at the base of the figure, offset from zero.

used. The transmission curves are also reported for completeness. As expected, the uncertainties in the NIR bands are larger, due to the larger scatter and systematic features in the light curves.

Inspection of Fig. 5 shows that our measurements are unfortunately not sufficiently accurate to claim a clear variation of r_b along the seven passbands. Using the planetary system values reported in Table 6, we computed a one-dimensional model atmosphere of WASP-44 b, using the atmosphere code described in Fortney et al. (2005, 2008). The fully non-grey model uses the chemical equilibrium abundances of Lodders & Fegley (2002) and the opacity data base described in Freedman, Marley & Lodders (2008). The atmospheric pressure–temperature profile simulates planet-wide average conditions. We furthermore computed the transmission spectrum of the model using the methods described in Fortney et al. (2010).

At optical wavelengths, r_b appears to be slightly larger in r' and i' than g' and z'. This is as expected for a planet with an equilibrium temperature $T_{eq} \approx 1300$ K, due to the larger predicted radius around the Na and K lines. Although a similar effect is seen in the model (Fig. 6), our data are not sufficiently precise to reject the default hypothesis that r_b is constant with wavelength. The radius of WASP-44 b is in agreement with the theoretical model in the J band, but is larger in the H and K bands. We found that the r_b in r' is 9.5 and 4.7 per cent smaller than that for the H and K bands, respectively, which correspond to a difference in units of atmospheric pressure scale height (H) of roughly $23H$ and $10H$, respectively. The first difference is very large, and would involve an extreme opacity in H.

A more plausible alternative is that the NIR photometry is affected by systematics or correlated noise, which was not possible to eliminate. This is also suggested by the poor SNR observed in the data, which is reflected in the higher scatter of the points in the J, H, K light curves and the different shapes of the fit in the same band between the first and the second observed transits (Figs 2 and 3). We deduce that systematic errors in the NIR dominate the error budget at these wavelengths.

4 SUMMARY AND DISCUSSION

In this work we have presented the first photometric follow-up of the transiting extrasolar planetary system WASP-44. One transit was observed using WFC on the INT, and two transits were observed in seven passbands simultaneously using GROND on the MPG/ESO 2.2 m telescope. Using these new data sets plus another one taken from the literature (Anderson et al. 2012), we have obtained improved measurements of the orbital ephemerides and physical properties of the system. In particular, we found that the radius of WASP-44 b is smaller than previously found, and is different (at the 2σ confidence level) from that theoretically expected for a core-free planet (Fortney et al. 2007). This suggests that

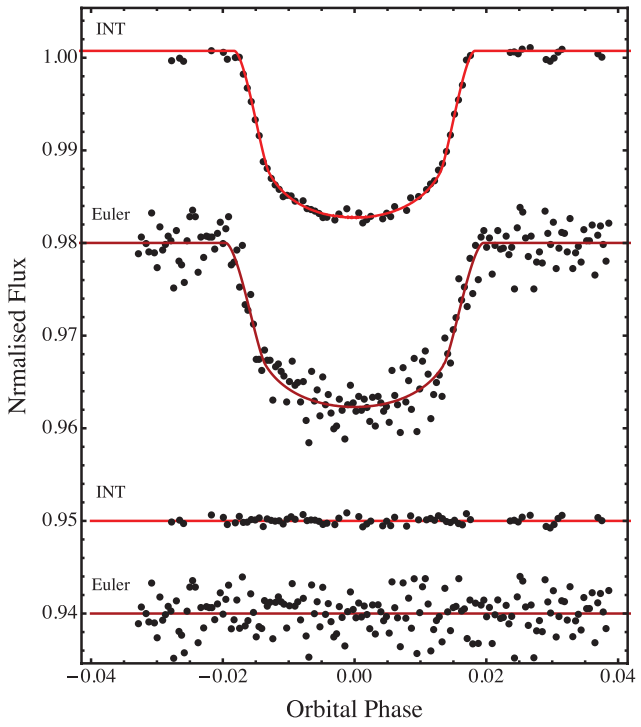

Figure 4. Same as for Fig. 2 but for the *r* filter INT and Euler (Anderson et al. 2012) light curves of WASP-44.

WASP-44 b is a 'heavy element rich' planet, with the heavy elements being in a distinct core or mixed within the H/He envelope. Such a result is important in order to draw an accurate *mass–radius* plot for TEPs, which provides key diagnostic for theoretical works that look to infer the bulk composition of the giant planets and distinguish them (in some cases) from brown dwarfs.

Although GROND was not designed for follow-up studies of planetary transits, it is one of the very few imaging systems worldwide able to perform simultaneous photometric multi-band observations. The latter fact makes GROND an efficient and very useful instrument to detect transit anomalies or to probe the atmosphere of TEPs. Indeed, atomic and molecular absorption as well as scattering processes may result in detectable radius variations as a function of wavelength (Fortney et al. 2007; Batygin et al. 2009). de Mooij et al. (2012) already used GROND in the case of GJ 1214 b, but they restricted their analysis only to the optical bands. Here, for the first time, we used all the seven bands of this powerful instrument, to search for variations of the radius of WASP-44 b with wavelength.

Table 6. Final physical properties of the WASP-44 system. The first error bar for each parameter is the statistical error, which stems from the measured spectroscopic and photometric parameters. The second error bar is the systematic error arising from the use of theoretical stellar models, and is given only for those parameters which have a dependence on stellar theory. The results from Anderson et al. (2012) are included for comparison.

	This work (final)	Anderson et al. (2012)
M_A ($M_\odot$)	$0.917 \pm 0.077 \pm 0.051$	0.951 ± 0.034
R_A ($R_\odot$)	$0.865 \pm 0.025 \pm 0.016$	$0.927^{+0.068}_{-0.074}$
$\log g_A$ (cgs)	$4.526 \pm 0.018 \pm 0.008$	$4.481^{+0.068}_{-0.057}$
ρ_A ($\rho_\odot$)	1.414 ± 0.058	$1.19^{+0.32}_{-0.22}$
M_b (M_{jup})	$0.869 \pm 0.075 \pm 0.032$	0.889 ± 0.062
R_b (R_{jup})	$1.002 \pm 0.033 \pm 0.018$	1.14 ± 0.11
g_b (m s^{-2})	21.5 ± 1.6	$15.7^{+3.4}_{-3.0}$
ρ_b (ρ_{jup})	$0.808 \pm 0.072 \pm 0.015$	$0.61^{+0.23}_{-0.15}$
T_{eq} (K)	1304 ± 37	1343 ± 64
Θ	$0.0652 \pm 0.0048 \pm 0.0012$	–
a (au)	$0.034\,45 \pm 0.000\,93 \pm 0.000\,63$	$0.034\,73 \pm 0.000\,41$
Age (Gyr)	$4.1^{+5.9}_{-6.0}{}^{+4.1}_{-2.4}$	–

We measured the planetary radius in the seven GROND passbands, corresponding to a wavelength coverage of 370–2440 nm, and compared them to a synthetic spectrum based on an isothermal model atmosphere in chemical equilibrium. The model reproduces the radius values in the optical, in agreement with the equilibrium temperature of WASP-44 b, but our data lack the precision to rule out the possibility that the planetary radius does not vary with wavelength. It does not predict the radius values found in the *H* and *K* bands, which differ by roughly 23 and 10 atmospheric pressure scale heights to those in the other bands. This phenomenon is most likely due to the comparatively low quality of the NIR data. We have worked to reduce the sources of noise in the subsequent uses of the GROND instrument. More enticing results were obtained for other TEPs and will be shown in forthcoming papers.

ACKNOWLEDGEMENTS

Based on observations collected at the MPG/ESO 2.2 m telescope located at ESO La Silla, Chile. Operations of this telescope are jointly performed by the Max Planck Gesellschaft and the European Southern Observatory. GROND has been built by the high-energy group of MPE in collaboration with the LSW Tautenburg and ESO, and is operating as a PI instrument at the MPG/ESO 2.2 m telescope. We thank David Anderson for supplying photometric data, and Timo Anguita and Régis Lachaume for their technical assistance

Table 5. Derived physical properties of WASP-44 from using each of five different theoretical stellar models. In each case $g_b = 21.5 \pm 1.6$ m s^{-2}, $\rho_A = 1.414 \pm 0.058$ $\rho_\odot$ and $T_{eq} = 1304 \pm 37$ K.

	This work (Claret models)	This work (Y^2 models)	This work (Teramo models)	This work (VRSS models)	This work (DSEP models)
K_b (km s^{-1})	156.1 ± 4.1	151.7 ± 1.0	152.6 ± 4.2	152.7 ± 4.1	153.7 ± 3.2
M_A ($M_\odot$)	0.968 ± 0.077	0.888 ± 0.018	0.904 ± 0.074	0.907 ± 0.073	0.924 ± 0.058
R_A ($R_\odot$)	0.881 ± 0.025	0.856 ± 0.016	0.862 ± 0.024	0.862 ± 0.024	0.865 ± 0.020
$\log g_A$ (cgs)	4.534 ± 0.018	4.521 ± 0.010	4.524 ± 0.018	4.524 ± 0.018	4.530 ± 0.016
M_b (M_{jup})	0.901 ± 0.075	0.851 ± 0.056	0.861 ± 0.073	0.863 ± 0.073	0.874 ± 0.067
R_b (R_{jup})	1.020 ± 0.033	0.992 ± 0.019	0.997 ± 0.033	0.998 ± 0.032	0.994 ± 0.027
ρ_b (ρ_{jup})	0.793 ± 0.070	0.816 ± 0.069	0.812 ± 0.072	0.811 ± 0.072	0.831 ± 0.071
Θ	0.0640 ± 0.0046	0.0658 ± 0.0045	0.0654 ± 0.0048	0.0654 ± 0.0047	0.0656 ± 0.0046
a (au)	$0.035\,08 \pm 0.000\,93$	$0.034\,09 \pm 0.000\,23$	$0.034\,29 \pm 0.000\,93$	$0.034\,32 \pm 0.000\,92$	$0.034\,54 \pm 0.000\,72$

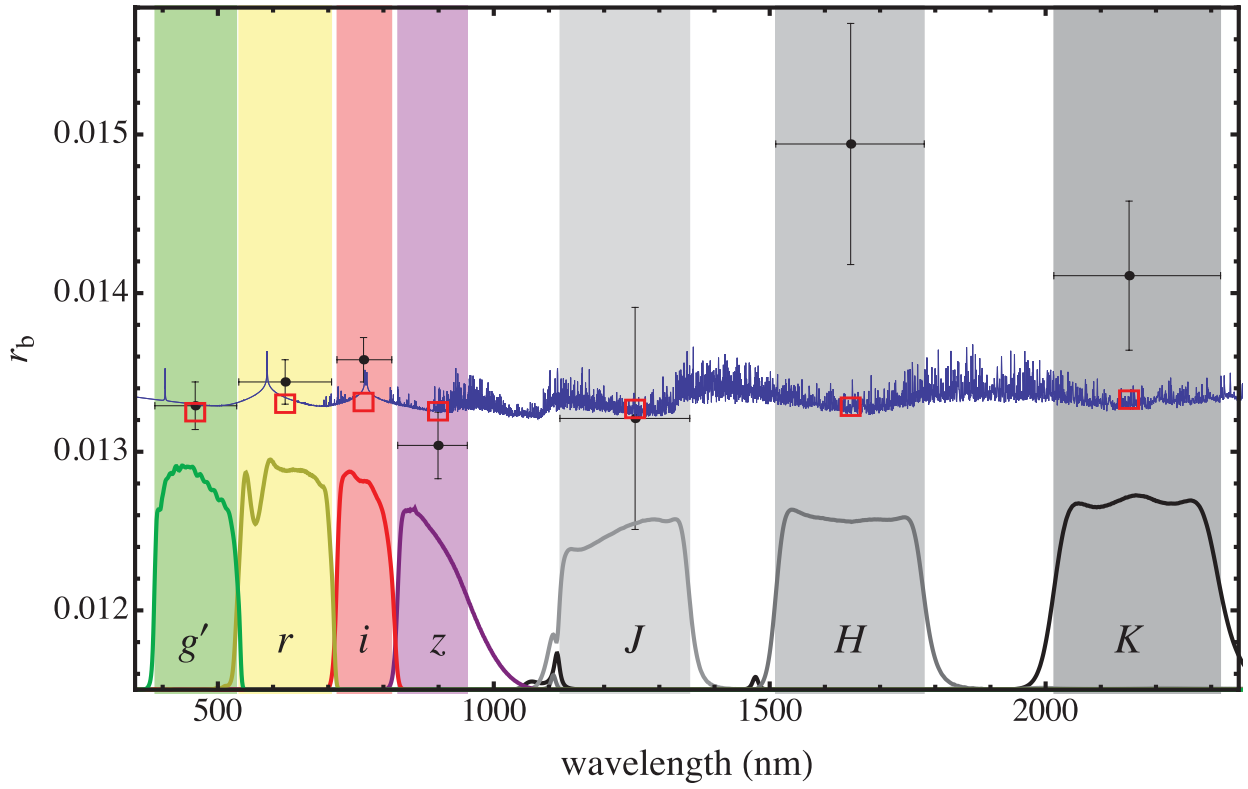

Figure 5. Variation of the fractional planetary radius $r_b = R_b/a$ with wavelength. The points shown in the plot are from the MPG/ESO 2.2 m telescope. The vertical bars represent the errors in the measurements, and the horizontal bars show the full width at half maximum transmission of the passbands used. The solid, blue continuous line denotes the calculated synthetic spectrum based on a theoretical model of the atmosphere of WASP-44 b. The red boxes indicate the predicted values for this model integrated over the passbands of the observations. Transmission curves of the GROND filters are shown at the bottom of the figure.

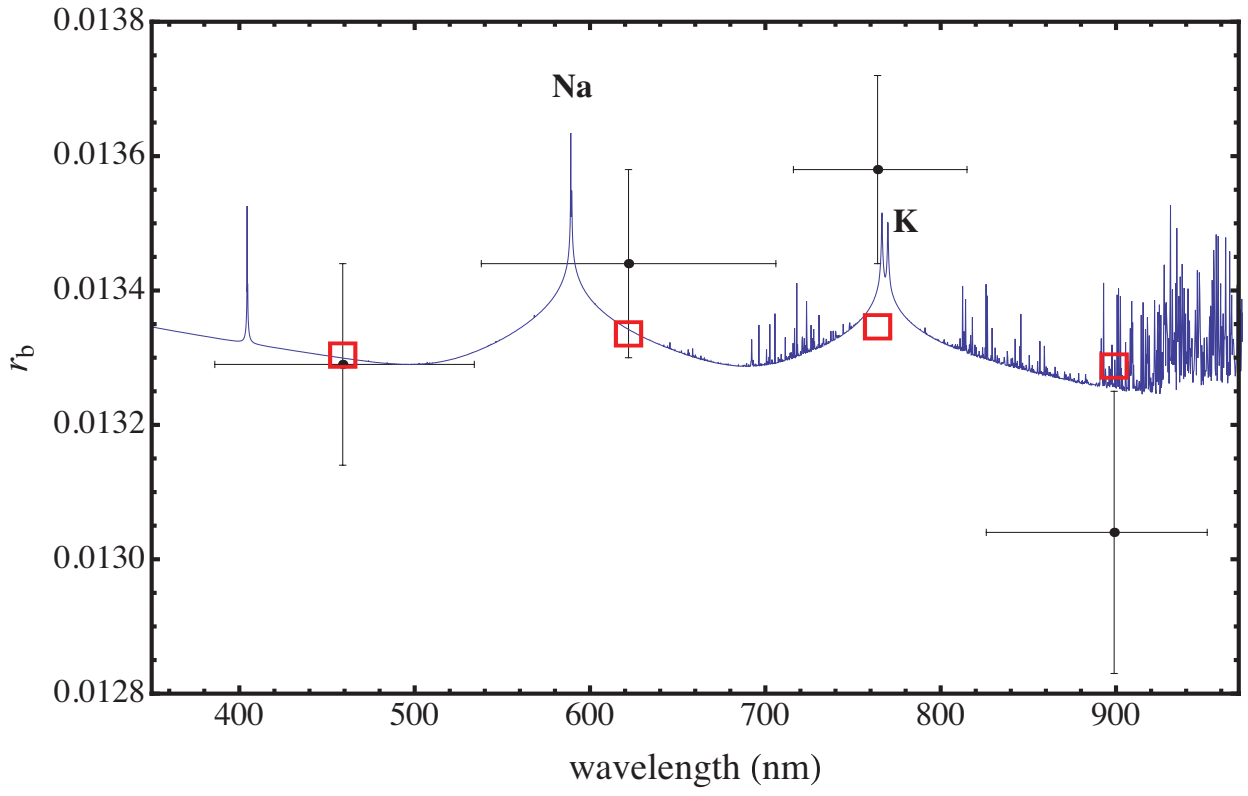

Figure 6. Same as in Fig. 5 but zoomed in on the optical wavelengths. In this range, the synthetic transmission spectrum is dominated by gaseous Na and K.

during the observations. We also thank the anonymous referee for their useful criticisms and suggestions that helped us to improve the quality of this paper. The reduced light curves presented in this work will be made available at the CDS (http://cdsweb.u-strasbg.fr/). JS acknowledges financial support from STFC in the form of an Advanced Fellowship.

REFERENCES

Anderson D. R. et al., 2012, MNRAS, 422, 1988
Andrae R., 2010, ApJ, preprint (arXiv:1009.2755)
Bakos G. Á. et al., 2012, AJ, 144, 19
Ballester G. E., Sing D. K., Herbert F., 2007, Nat, 445, 511
Barman T., 2007, ApJ, 661, L191
Batalha N. M. et al., 2013, ApJS, 204, 24
Batygin K., Bodenheimer P., Laughlin G., 2009, ApJ, 704, L49
Bean J. L. et al., 2011, ApJ, 743, 92
Beatty T. G. et al., 2012, ApJ, 756, L39
Beaulieu J. P., Carey S., Ribas I., Tinetti G., 2008, ApJ, 677, 1343
Beaulieu J. P. et al., 2010, MNRAS, 409, 963
Beaulieu J. P. et al., 2011, ApJ, 731, 16
Bodenheimer P., Laughlin G., Lin D. N. C., 2003, ApJ, 592, 555
Borucki W. J. et al., 2011a, ApJ, 728, 117
Borucki W. J. et al., 2011b, ApJ, 736, 19
Boss A. P., 1997, Sci, 276, 1836
Brown T. M., 2001, ApJ, 553, 1006
Bryan M. L. et al., 2012, ApJ, 750, 84
Burrows A., Hubeny I., Budaj J., Hubbard W. B., 2007, ApJ, 661, 502
Burrows A., Rauscher E., Spiegel D. S., Menou K., 2010, ApJ, 719, 341
Charbonneau D., Brown T. M., Noyes R. W., Gilliland R. L., 2002, ApJ, 568, 377
Charbonneau D. et al., 2005, ApJ, 626, 523
Claret A., 2004, A&A, 428, 1001
Colón K. D., Ford E. B., Redfield S., Fortney J. J., Shabram M., Deeg H. J., Mahadevan S., 2012, MNRAS, 419, 2233
Crossfield I. J. M., Barman T., Hansen B. M. S., 2011, ApJ, 736, 132
Crossfield I. J. M., Knutson H., Fortney J., Showman A. P., Cowan N. B., Deming D., 2012, ApJ, 752, 81
Crouzet N., McCullough P. R., Burke C. J., Long D., 2012, ApJ, 761, 7
D'Angelo G., Durisen R. H., Lissauer J. J., 2010, in Seager S., ed., Exoplanets. Univ. Arizona Press, Tucson, AZ, p. 319
de Mooij E. J. W. et al., 2012, A&A, 538, A46
Deming D., Brown T. M., Charbonneau D., Harrington J., Richardson L. J., 2005, ApJ, 622, 1149
Demory B.-O., Seager S., 2011, ApJS, 197, 12
Désert J.-M., Vidal-Madjar A., Lecavelier Des Etangs A., Sing D., Ehrenreich D., Hébrard G., Ferlet R., 2008, A&A, 492, 585
Désert J.-M. et al., 2011, A&A, 526, A12
Dobbs-Dixon I., Lin D. N. C., 2008, ApJ, 673, 513
Eastman J., Silverd R., Gaudi B. S., 2010, PASP, 122, 935
Fortney J. J., Marley M. S., Lodders K., Saumon D., Freedman R., 2005, ApJ, 627, L69
Fortney J. J., Marley M. S., Barneset J. W., 2007, ApJ, 659, 1661
Fortney J. J., Lodders K., Marley M. S., Freedman R. S., 2008, ApJ, 678, 1419
Fortney J. J., Shabram M., Showman A. P., Lian Y., Freedman R. S., Marley M. S., Lewis N. K., 2010, ApJ, 709, 1396
Fossati L. et al., 2010, ApJ, 714, L222
Freedman R. S., Marley M. S., Lodders K., 2008, ApJ, 174, 513
Gaudi B. S., 2005, ApJ, 628, 73
Gibson N. P. et al., 2008, A&A, 492, 603
Gibson N. P., Pont F., Aigrain S., 2011, MNRAS, 411, 2199
Gibson N. P. et al., 2012, MNRAS, 422, 753
Gibson N. P., Aigrain S., Barstow J. K., Evans T. M., Fletcher L. N., Irwin P. G. J., 2013, MNRAS, 428, 3680
Gillon M., Pont F., Moutou C., Bouchy F., Courbin F., Sohy S., Magain P., 2006, A&A, 459, 249
Gillon M. et al., 2012, A&A, 539, A28
Greiner J. et al., 2008, PASP, 120, 405
Gu P.-G., Bodenheimer P. H., Lin D. N. C., 2004, ApJ, 608, 1076
Hartman J. D. et al., 2012, AJ, 144, 139
Hellier C. et al., 2012, MNRAS, 426, 739
Hilditch R. W., 2001, An Introduction to Close Binary Stars. Cambridge Univ. Press, Cambridge
Holman M. J., Murray N. W., 2005, Sci, 307, 1288
Hubbard W. B., Fortney J. J., Lunine J. I., Burrows A., Sudarsky D., Pinto P., 2001, ApJ, 560, 413
Ibgui L., Burrows A., 2009, ApJ, 700, 1921
Ibgui L., Burrows A., Spiegel D. S., 2010, ApJ, 713, 751
Jackson B., Greenberg R., Barnes R., 2008, ApJ, 681, 1631
Knutson H. A., Charbonneau D., Noyes R. W., Brown T. M., Gilliland R. L., 2007a, ApJ, 655, 564
Knutson H. A. et al., 2007b, Nat, 447, 183
Laughlin G., Crismani M., Adams F. C., 2011, ApJ, 729, 7
Lecavelier des Etangs A., Vidal-Madjar A., Désert J.-M., Sing D., 2008, A&A, 485, 865
Lodders K., Fegley B., 2002, Icarus, 155, 393
Lubow S. H., Ida S., 2010, in Seager S., ed., Exoplanets. Univ. Arizona Press, Tucson, AZ, p. 347
Mancini L. et al., 2013, A&A, 551, A11
Mayor M., Queloz D., 1995, Nat, 378, 355
Miller N., Fortney J. J., 2011, ApJ, 736, L29
Miller N., Fortney J. J., Jackson B., 2009, ApJ, 702, 1413
Nikolov N., Henning Th., Koppenhoefer J., Lendl M., Maciejewski G., Greiner J., 2012, A&A, 539, 159
Nikolov et al., 2013, A&A, in press
Penev K. et al., 2013, AJ, 145, 5
Pollack J. B., Hubickyj O., Bodenheimer P., Lissauer J. J., 1996, Icarus, 124, 62
Pont F., Zucker S., Queloz D., 2006, MNRAS, 373, 231
Pont F., Knutson H., Gilliland R. L., Moutou C., Charbonneau D., 2008, MNRAS, 385, 109
Redfield S., Endl M., Cochran W. D., Koesterke L., 2008, ApJ, 673, L87
Richardson L. J., Harrington J., Seager S., Deming D., 2006, ApJ, 649, 1043
Richardson L. J., Deming D., Horning K., Seager S., Harrington J., 2007, Nat, 445, 892
Seager S., Mallén-Ornelas G., 2003, ApJ, 585, 1038
Seager S., Sasselov D. D., 2000, ApJ, 537, 916
Sing D. K., Vidal-Madjar A., Désert J.-M., Lecavelier des Etangs A., Ballester G., 2008a, ApJ, 686, 658
Sing D. K., Vidal-Madjar A., Lecavelier des Etangs A., Désert J.-M., Ballester G., Ehrenreich D., 2008b, ApJ, 686, 667
Sing D. K. et al., 2011a, MNRAS, 416, 1443
Sing D. K. et al., 2011b, A&A, 527, A73
Sing D. K. et al., 2012, MNRAS, 426, 1663
Siverd R. J. et al., 2012, ApJ, 761, 123
Smalley B. et al., 2012, A&A, 547, 61
Snellen I. A. G., Albrecht S., de Mooij E. J. W., Le Poole R. S., 2008, A&A, 487, 357
Snellen I. A. G., de Kok R. J., deMooij E. J. W., Albrecht S., 2010, Nat, 465, 1049
Southworth J., 2008, MNRAS, 386, 1644
Southworth J., 2009, MNRAS, 394, 272
Southworth J., 2010, MNRAS, 408, 1689
Southworth J., 2011, MNRAS, 417, 2166
Southworth J., 2012, MNRAS, 426, 1291
Southworth J., Maxted P. F. L., Smalley B., 2005, A&A, 429, 645
Southworth J., Wheatley P. J., Sams G., 2007, MNRAS, 379, L11
Southworth J. et al., 2009, MNRAS, 396, 1023
Southworth J., Bruni I., Mancini L., Gregorio J., 2012a, MNRAS, 420, 2580
Southworth J., Mancini L., Maxted P. F. L., Bruni I., Tregloan-Reed J., Barbieri M., Ruocco N., Wheatley P. J., 2012b, MNRAS, 422, 3099
Spiegel D. S., Silverio K., Burrows A., 2009, ApJ, 699, 1487
Stetson P. B., 1987, PASP, 99, 191
Sudarsky D., Burrows A., Pinto P., 2000, ApJ, 538, 885

Sudarsky D., Burrows A., Hubeny I., 2003, ApJ, 588, 1121
Swain M. R., Vasisht G., Tinetti G., 2008, Nat, 452, 329
Tinetti G. et al., 2007, Nat, 448, 169
Tinetti G., Deroo P., Swain M. R., Griffith C. A., Vasisht G., Brown L. R., Burke C., McCullough P., 2010, ApJ, 712, L139
Vidal-Madjar A., Lecavelier des Etangs A., Désert J.-M., Ballester G. E., Ferlet R., Hébrard G., Mayor M., 2003, Nat, 422, 143
Vidal-Madjar A. et al., 2004, ApJ, 604, L69
Winn J. N. et al., 2005, ApJ, 631, 1215
Winn J. N. et al., 2007, AJ, 134, 1707
Winn J. N. et al., 2008, ApJ, 683, 1076
Winn J. N., Holman M. J., Carter J. A., Torres G., Osip D. J., Beatty T., 2009, AJ, 137, 3826
Wood P. L., Maxted P. F. L., Smalley B., Iro N., 2011, MNRAS, 412, 2376
Zahnle K., Marley M. S., Freedman R. S., Lodders K., Fortney J. J., 2009, ApJ, 701, L20

APPENDIX A: GROND NIR DATA REDUCTION

The calibration of the GROND NIR data is a little more complicated than the optical data, because of the presence of electronic odd–even readout pattern along the *y*-axis. In order to remove this pattern, we smooth each image and compare it with the unsmoothed ones after the master dark has been subtracted. The amplitudes of the readout pattern are then determined by comparing the median level of each column to the overall median level. Each column is shifted back to the overall median level. The master sky flats are divided out from the science images after the removal of the readout pattern.

Since our observations are in staring mode, sky background is an important contribution in the images. With the 20-position dithering sky measurements right before and after the science time series, we could construct a sky emission model for each science image. These sky images are calibrated in the same way as the science images. We mask out all the stars in the calibrated sky images, and normalize each image with their own overall median levels. All the normalized skies are then median-combined, and normalized again. For each science image, we scale the pre- and post-science sky models to their background individually. The final sky model is constructed by weighted combining them according to the inverse square of fitted χ^2. This sky model is then subtracted from a corresponding science image. After sky subtraction, we still see remnant structure, which is expected due to the variation of the sky during the observing sequence.

After these calibrations have been applied, we perform aperture photometry on WASP-44 as well as three nearby comparison stars. The locations of each star are determined by IDL/FIND, which calculates the centroids by fitting Gaussians to the marginal x and y distributions. In order to find the optimal photometry, we lay 30 apertures on all the stars in a step of 0.5 pixel, each with 10 annuli in a step of 1 pixel. This produces 300 data sets with different aperture settings. In this way, the above-mentioned sky subtraction remnant effect is accounted for in the sky annulus adopted in the aperture photometry. We divide the flux of each star with its own median value. A composite reference light curve is constructed by median-combining fluxes of ensembles of comparison stars, which are required to show the least deviation from the target. We normalize the target light curve with this composite reference light curve.

Since the normalized light curve still shows strong red noise correlated with positions, seeing and airmass, instead of selecting the optimal photometry directly from the rms of an out-of-transit baseline, we fit the whole light curve simultaneously with the theoretical light curve model multiplied with a baseline correction function. This correction function consists of positions/time in quadratic form, and FWHMs/airmass in linear form. We tried to select the optimal light curves by choosing the ones with the least rms of O−C flux residuals among all the data sets. However, the transit depths of the optimal light curves of the same band from different nights are very deviant from each other. We note that light curves of the same band obtained using different aperture and annulus sizes could exhibit a similar least rms, however produce different transit depths. Therefore, for each NIR band, we choose the two light curves with the least rms and with consistent transit depth between the two nights as our final optimal photometric results.

This paper has been typeset from a TEX/LATEX file prepared by the author.